Journal of Micromechanics and Microengineering

Frequency tunable resonant magnetoelectric sensors for the detection of weak magnetic field

OPEN ACCESS
IOP Publishing
Made open access 5 August 2020
Journal of Micromechanics and Microengineering
J. Micromech. Microeng. **30** (2020) 075009 (8pp)
https://doi.org/10.1088/1361-6439/ab8dd0

Frequency tunable resonant magnetoelectric sensors for the detection of weak magnetic field

Jingxiang Su[1], Florian Niekiel[1], Simon Fichtner[1,2], Christine Kirchhof[2], Dirk Meyners[2], Eckhard Quandt[2], Bernhard Wagner[1,2] and Fabian Lofink[1]

[1] Fraunhofer Institute for Silicon Technology ISIT, Fraunhoferstrasse 1 25524, Itzehoe, Germany
[2] Institute for Material Science, Kiel University, Kaiserstrasse 2 24143, Kiel, Germany

E-mail: jingxiang.su@isit.fraunhofer.de

Received 13 January 2020, revised 13 March 2020
Accepted for publication 28 April 2020
Published 22 May 2020

Abstract

This paper reports on frequency tunable MEMS magnetoelectric (ME) sensors. Different designs are studied in respect to ME voltage coefficient and frequency tunability. Compared to state-of-the-art ME sensors, the presented ME resonators display a highly reversible and linear frequency tuning, enabled by applying a DC voltage to piezoelectric actuators. A frequency shift of up to 0.2 Hz V^{-1} is demonstrated for a sensor with a limit of detection of 128 pT/$Hz^{0.5}$ at resonance frequency of 13 kHz. This sensor type is of particular interest for vector field sensors and sensor arrays in bio-magnetic applications, where sensors with either identical resonance frequencies or precisely defined frequency spacing are required.

Keywords: MEMS, magnetoelectric sensor, piezoelectric, frequency tuning

Some figures may appear in colour only in the online journal

1. Introduction

MEMS sensors based on magnetoelectric (ME) composites have attracted great interest due to their capability to detect magnetic fields in the pT regime at low frequencies, showing a high potential in applications like biomagnetic field detection, magnetic particle imaging and antennas [1–5]. According to the current state of the art, superconducting quantum interference devices (SQUIDs) are the most commonly used ultra-high sensitive low-field magnetometers in biomedical applications like magneto-encephalography or -cardiography (MEG, MCG) [6]. However, the arrays of SQUIDs in MEG or MCG applications require a costly cooling system with liquid helium to minimize the instrumental noise and a shielded room for operation [7, 8]. Due to their bulky cooling system, SQUID sensors have a greater distance to the bio-magnetic source (i.e. the human brain or the human heart) than the room temperature sensors [7] and thus require a significantly better sensitivity for the same measurement task. Due to the aforementioned limitations of SQUIDs, MEMS ME sensors with small size, showing a high sensitivity in biomagnetic field detection at room temperature, are of particular interest [1, 9].

MEMS sensors based on ME composites are comprised of mechanically coupled magnetostrictive and piezoelectric materials. The presence of a magnetic field leads to a change in the strain of the magnetostrictive layer which is transferred to the piezoelectric material via the mechanical coupling. An electrical voltage across the piezoelectric layer is thus generated [10, 11]. As a figure of merit of ME sensors, ME voltage coefficient α_{ME} describes the change of the electric field in dependence of the magnetic field strength given by equation (1) [9]:

$$\alpha_{ME} = \frac{U_{ME}}{t_{piezo} \cdot H_{ac}} \tag{1}$$

where U_{ME} is the voltage ouput of the sensor, t_{piezo} is the thickness of the piezoelectric layer and H_{ac} is the applied alternating excitation magnetic field.

As the ME effect provides a high sensitivity already at room temperature, a cooling system can be omitted. MEMS ME sensors can be vacuum encapsulated using wafer-level packaging (WLP) technology which protects the sensors during handling and from environmental influences [12]. Moreover,

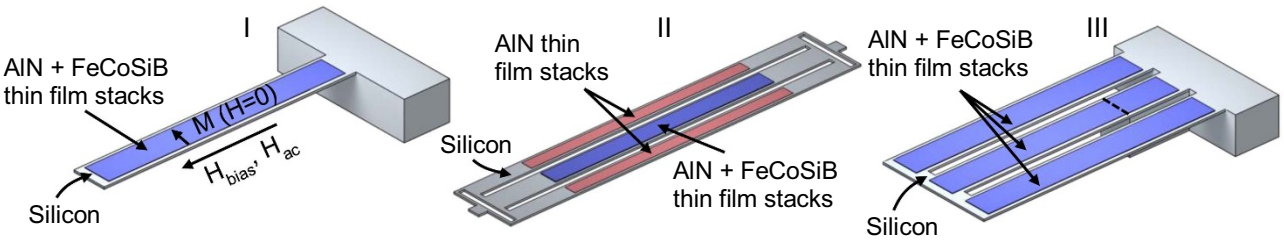

Figure 1. Schematic illustration of the reference and two tunable ME sensor concepts. The reference (sensor I) is a cantilever with geometry of 1500 μm $\times$ 200 μm. The substrate of sensor II contains an inner beam with a size of 2234 μm $\times$ 105 μm and two outer beams with a size of 2234 μm $\times$ 146 μm with a gap of 40 μm. The functional layers with a length of 1500 μm are deposited in the middle of the substrate. All three beams are mechanically coupled on both sides and decoupled from the substrate by introducing a stress relaxation structure. Sensor III consists of outer beams with the same size of 1500 μm $\times$ 200 μm and an inner beam of 1000 μm $\times$ 200 μm instead of 1500 μm $\times$ 200 μm due to the unfinished etch (the dotted line). The coupling structure of the sensor has a dimension of 100 μm $\times$ 700 μm and the gap between neighbouring beams is 50 μm.

the vacuum environment significantly reduces the laminar damping resulting in a higher quality factor Q [13, 14]. For the use in medical applications, WLP MEMS ME sensors have small size and thus can easily be assembled in flexible sensor arrays adapted to different diagnostic requirements.

Resonant thin film ME sensors exhibit a significant enhancement of the ME coefficient in resonance over a narrow bandwidth [15]. To enable wideband measurement and allow these sensors to measure low frequency signals, frequency conversion through AC magnetic [16, 17] or electric fields [17, 18] has been developed. For specific applications, the development of vector field sensors and sensor arrays requires either identical resonance frequencies or precisely defined frequency spacing. For instance, to detect the artificial magnetic signal of deep brain stimulation, the resonance frequency of ME sensor has to be tuned to the stimulus frequency of brain pacemaker or its higher harmonics [19]. To build up tuning fork ME sensors which are designed to reduce the acoustic noise, ME sensors with identical resonance frequencies are required [20]. These are just a few examples for which tunable sensors are a great help or even an enabler. It is therefore very important to fabricate sensors with exactly reproducible resonance frequencies. However, manufacturing tolerances typically in the order of few percent cannot be avoided and are far above the tolerable range in such applications which is the bandwidth Δf of the sensor. For high Q, the bandwidth of ME sensors $\Delta f = f_{res}/Q$ is typically in the per mill range or below. Thus, there is a need to develop ME sensors with the ability to tune their resonance frequency. Few resonance frequency tuning methods for ME sensors have been reported. Röbisch *et al* presented a ME sensor based on shape memory alloy substrate whose frequency is tuned by changing the microstructure of the substrate via temperature [21]. Petrie *et al* discussed a technique to tune the resonance frequency by applying an in-plane tensile force via a suspended weight [22]. Wang *et al* studied a frequency shift method for ME sensor via an inductor–capacitor (LC) circuit [23].

In this paper, we present two vacuum encapsulated tunable ME sensors with integrated piezoelectric actuators (figure 1(II) and (III)) [24]. A standard design cantilever ME sensor using the same fabrication technology is presented as a reference (figure 1(I)). It is the first time that a low-stress polycrystalline silicon (poly-Si) layer as a substrate is integrated into ME sensors using surface micromachining process. As the amorphous magnetostrictive material FeCoSiB used in this work is temperature sensitive and its crystallization happens at a temperature above 350 °C [25], a wafer level AuSn transient liquid phase (TLP) bonding process [12] with low bonding temperature of 330 °C is applied.

The paper is organized as follows: first, the sensor concepts are discussed in section 2. In section 3, the fabrication and the measurement setup are presented. Then the characterization results of the tunable sensors are discussed and compared to the reference sensor in section 4. Finally a conclusion is given.

2. Sensor concepts

Simplified schematic illustrations of the ME sensors are sketched in figure 1. The reference (sensor I) is a clamped-free cantilever with a poly-Si layer (12 μm) as substrate and ME composites consisting of AlN (1 μm)/FeCoSiB (2 μm). In the previous technology, ME sensors are designed based on a 650 nm thin SiO_2 substrate [11, 13]. These sensors face problems like low quality factor Q and undesired bending of the structure due to residual stress in the functional layers. Here, a 12 μm thick low-stress poly-Si substrate is integrated to ME sensors using surface micromachining process as we have extensive in-house processing experience of polycrystalline silicon. The introduction of the poly-Si layer increases the Q factor and reduces the impact of the stress from other layers on ME sensors. It also reduces the requirements for adjusting the intrinsic mechanical stress of the ME functional layers. Moreover, a great design flexibility is given by a stiff elastic substrate providing the possibility to realize mechanically coupled resonators. The deposited magnetostrictive layer has a magnetic easy axis along the short axis of the cantilever (figure 1(I)). Applying a magnetic bias field H_{bias} and an alternating magentic field H_{ac} pointing to the long axis of

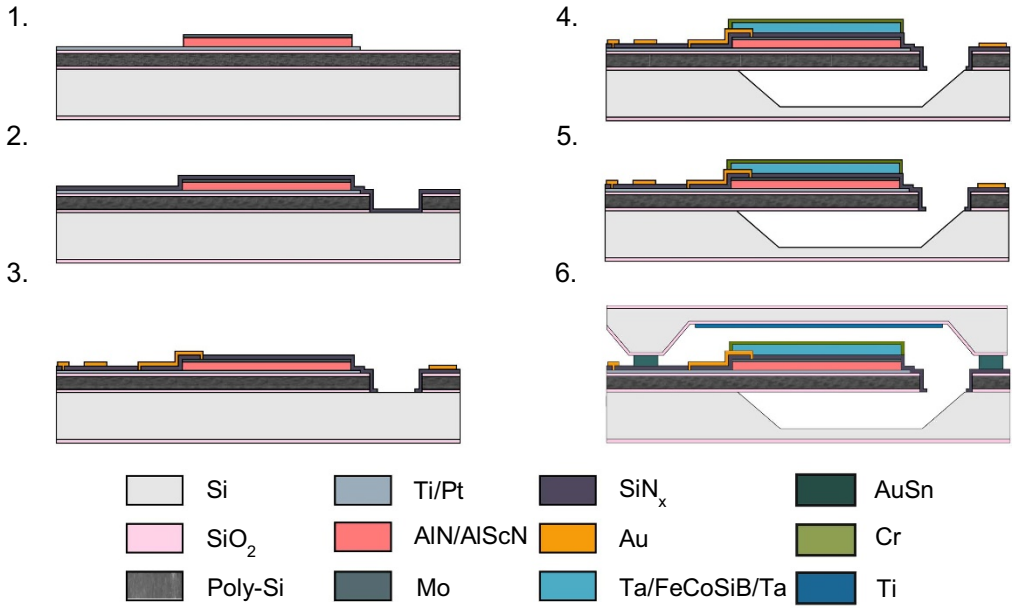

Figure 2. Process flow of the ME sensors. Step 1: a piezoelectric stack of Ti/Pt/AlN/Mo is deposited on the poly-Si device layer; step 2: a thin passivation layer (SiN_x) is introduced; step 3: the contact pads, the contact lines and the bond frames (4 μm Au) are electroplated using Ti/Au as electrode plating base after dry etching of the openings of SiN_x; step 4: a thin Cr layer is deposited to protect the structured magnetic layer from chemical attack; step 5: MEMS resonators are obtained after anisotropic TMAH etching of silicon; step 6: the schematic cross-section of the vacuum-encapsulated MEMS ME sensors.

the cantilever shifts the operating point in the magnetostriction curve. At optimal magnetic bias field H_{bias}, where the derivative of the magnetostriction with respect to the applied magnetic field reaches its maximum, a maximum ME voltage coefficient is reached [9].

Sensor II is a double-side clamped coupled resonator. The middle beam with a stack of poly-Si/AlN/FeCoSiB is used as the magnetic field sensing element for piezoelectric readout. The outer piezoelectric actuator beams consist of poly-Si and the piezoelectric layer (AlN). An applied DC voltage to the outer beams leads to a displacement of the piezoelectric layer via the inverse piezoelectric effect. As the piezoelectric layer is coupled to a thick poly-Si layer with high stiffness, a stress induced by the displacement is generated in the outer beams. As all three beams are mechanically coupled and clamped on both sides, the displacement-induced stress is transfered to the whole structure. The resonance frequency is tuned by changing the stress in the structure via the applied voltage. In comparison to sensor I, a reduced sensitivity but a distinct frequency shift is expected for sensor II because the double-sided clamped structure limits the bending but also reduces stress relaxation.

To increase sensitivity, sensor III is designed as a clamped-free structure consisting of three parallel cantilevers. All three beams have exactly the same stack with the reference (sensor I) to achieve a comparable performance. To enable tuning, the actuators (outer cantilevers) and the sensing element (inner cantilever) are coupled via a poly-Si bar at the tip of the cantilevers. Similarly, the output voltage of the centre beam responding to the AC magnetic field is recorded, and the outer beams are used as piezoelectric actuators. The resonance frequency of sensor III can be tuned by applying a voltage to the outer beams to change the beam stiffness.

3. Experimental methods

3.1. Sample fabrication

ME sensors have been fabricated using a surface micromachining process. All three ME sensors presented in this paper are manufactured on the same wafer. The process flow of the device is presented in figure 2.

The process of the device wafer starts with the deposition of a polished 12 μm thick low stress poly-Si layer on an oxidized Si wafer. After the deposition of an additional PECVD SiO_2 isolation layer (650 nm), the bottom electrode with 20 nm Ti and 100 nm Pt is evaporated and structured by a lift-off process. The next step is to sputter deposit 1 μm piezoelectric layer of AlN and 100 nm Mo as top electrode. The wet etching of AlN is performed in tetramethylammonium hydroxide (TMAH) at 82 °C using the structured Mo as a hard mask (figure 2(1)). A low stress passivation layer SiN_x with a thickness of 1 μm is introduced after the deep reactive-ion etching (DRIE) of poly-Si for the cavity openings (figure 2(2)). Dry etching is used to define the openings of SiN_x to the electrodes, enabling the connection to the contact pads via Au conduction lines. The bond frames with a thickness of 4 μm Au are electroplated at the same time with the contact pads and contact lines (4 μm) using Ti/Au as electrode plating base (figure 2(3)). A stack of Ta (10 nm)/FeCoSiB (2 μm)/Ta (50 nm) is sputter deposited under a magnetic field and structured by ion beam etching. After a 100 nm Cr layer is sputtered to protect

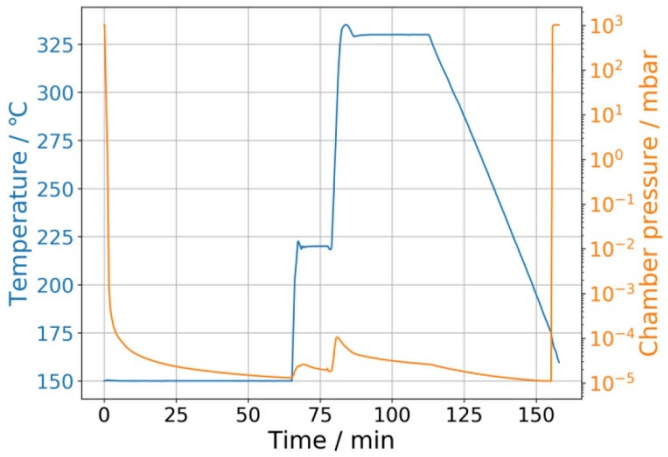

Figure 3. Temperature and chamber pressure during the bonding process. The bonding process starts at 150 °C and the temperature is increased to at 220 °C for degassing after 1 h. The wafers are then brought into contact at 330 °C for 30 min and cooled down. The whole bonding process takes place under a pressure of 5×10^{-5} mbar.

the magnetic layer from chemical attack (figure 2(4)), MEMS resonators are finally released by anisotropic TMAH etching of the Si substrate from the front side (figure 2(5)). After 6 h etching, sensor I and II are completely released, while in the case of sensor III one third of the middle beam is still fixed to the substrate (compared to the dotted line in figure 1(III)). A longer etching time is not preferred here because there is a high risk that the structures might be destroyed. Even though the inner beam of sensor III is not completely released in this case, the performance of the sensor is not expected to change significantly except a higher resonance frequency.

The cap wafer cavities are etched by KOH using PECVD SiN_x as a hard mask. Followed by the removal of the hard mask, a 650 nm SiO_2 is grown on the cap wafer. In the next step, the bond frames with 4 μm Au and 3 μm Sn are electroplated using a Ti/Au plating base. 400 nm thick Ti getter material is deposited into the cap wafer cavities and structured by a lift-off procedure.

The vacuum encapsulation is performed using a wafer-level AuSn TLP bonding process [12]. The temperature and the chamber pressure during the bonding process are plotted in figure 3. After the alignment of the cap and the device wafers, the chamber of the wafer bonder is pumped down to 5×10^{-5} mbar at 150 °C. After one hour, the system is heated up to 220 °C for degassing and held at this temperature for 10 min. Then the wafers are brought into contact and the system is further heated up to 330 °C for another 30 min. As this temperature is above the melting point of Sn, the interlayer Sn melts and diffuses to the neighbor solid layers resulting in an isothermal solidification. After the bonding time of 30 min, the wafers are cooled down and unloaded. Although the titanium getter is only fully activated at a temperature of 400 °C or after significantly longer annealing times, the generated getter capacity is sufficient to increase the Q factor by about one order of magnitude [14]. To get the sensor elements (figure 2(6)), the cap wafer and the device wafer are diced in sequence. At the end, the sensors are assembled for characterization using wire bonding. The photographs of the presented tunable ME sensors before and after vacuum encapsulation are shown in figure 4.

3.2. Measurement setup

The characterization of the sensors is done in a shielded measurement setup (figure 5). The sensor is placed into a tube surrounded by two coils. One coil is used to generate the homogenous bias static magnetic field and the other for the homogenous alternating excitation magnetic field. The magnetic fields generated by the coils have been calibrated using a Hall sensor. During the calibration, the Hall sensor is placed in the same position of the sample offline. In the frequency range from 7 kHz to 14 kHz, the uncertainty of the magnitude of the magnetic fields generated by the coils is about 1%. To shield the sensor from environmental acoustic and electromagnetic disturbances, the sensor and the coils are enclosed by several layers of thin mu-metal foil and placed inside an electrically shielded box lined with acoustic absorber. The readout and excitation devices are located outside the box.

The current for the magnetic bias field is generated by a Keithley 2614B sourcemeter. A SRS CS580 voltage controlled current source together with an Agilent 33120A function waveform generator provides the current for the excitation magnetic field. Inside the shielded box, a low-noise junction gate field-effect transistor (JFET) charge preamplifier using the circuit from [26] is directly connected to the center beam of the sensor and the generated voltage in dependence of the bias magnetic field is measured in resonance with a lock-in amplifier SR830 from Stanford Research System. The intrinsic voltage noise density of the sensor is recorded by an audio interface (Behringer U-Phoria UMC404HD).

For the frequency tuning measurement, the voltage applied to the piezoelectric actuators (outer beams) is supplied by a Keithley 2400 sourcemeter. To determine the minimum detectable magnetic filed and linearity regime of the investigated sensor at tuning, the source is replaced by batteries with up to 50 V for providing a low-noise voltage supply.

4. Results and discussion

For all measurements of the tunable sensors shown below, the middle beam of the investigated tunable sensors is used as the magnetic field sensing element and measured at an optimal bias magnetic field and in resonance. The outer beams of the investigated sensors are used as piezoelectric actuators to tune the resonance frequency.

The shape of the in-plane magnetostrictive hysteresis loop is mainly determined by the induced anisotropy K during the deposition of FeCoSiB at magnetic field. As the material is soft magnetic in nature, the corresponding anisotropy value is very small so that even small changes in film stress can alter the direction of easy and hard magnetic axes. For the applied deposition process the stress distribution of the magnetic layer has a significant spread, so that K varies by $\pm 25\%$ over the wafer and thus the optimum bias field differs slightly for each

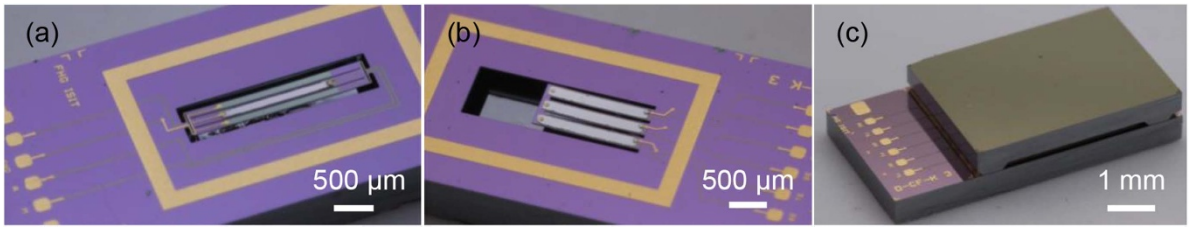

Figure 4. (a) and (b) Photographs of sensor II and III before vacuum encapsulation respectively; (c) shows the photograph of sensor III after vacuum encapsulation.

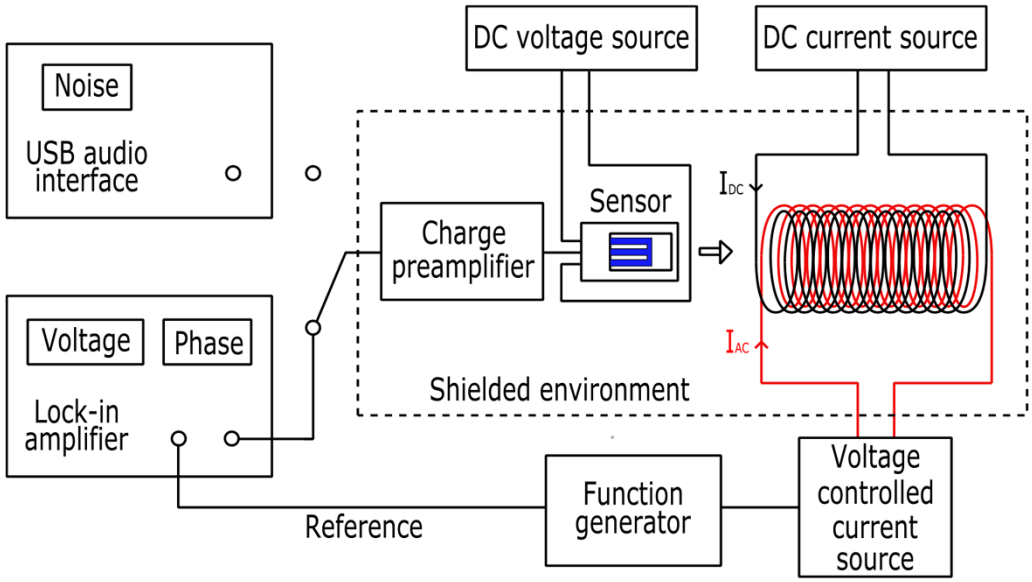

Figure 5. Schematic illustration of the measurement setup. The dashed line area indicates the magnetically and electrically shielded box. The bias magnetic field is generated by the coil drawn in black while the excitation field is generated by the coil drawn in red. The DC voltage source is used in the frequency tuning measurement for applying the voltage to the outer beams of the sensor.

sensor. From the preliminary investigations, the maximum ME voltage coefficient was achieved at a magnetic bias field μH_{bias} of 0.8 mT for sensor I, 0.5 mT for sensor II and 0.9 mT for sensor III. Operating at their optimal bias fields, the ME coefficients of all three sensors at resonance (when driven with an excitation magnetic field μH_{ac} of 1 μT) are shown in figure 6. It can be seen that all sensors show the highest ME coeficient at their mechanical resonance. The resonance frequencies f_{res} of 8200 Hz, 11 195 Hz and 13 043 Hz are measured for sensor I, II and III respectively. The resonance frequencies differ for all three sensors as they differ in designs. Considering the manufacturing tolerances, the resonance frequency of sensor I is in good agreement with finite element analysis (FEA) calculation (only considering the mechanical part of the sensor geometry). In contrast, the resonance frequencies of sensor II and III differ slightly from FEA results. This might due to the intrinsic stresses in the layers (most prominent in the magnetic layer). In resonance, the ME coefficients of 661 V cmOe^{-1} for sensor I, 22 V cmOe^{-1} for sensor II and of 424 V cmOe^{-1} for sensor III have been measured. A relative error of 5% is estimated for all three sensors from repeated measurements. It is mainly caused by the uncertainties of the magnetic fields generated by the coils and positioning, i.e. aligning the sensors within the coils. The Q factors of about 1800, 1600 and 1900 are determined from the bandwidth for sensor I, II and III, respectively. Among all devices, sensor II has a significantly smaller ME coefficient due to the limited bending of its double-side clamped structure. Between the clamped-free cantilevers with the same length, sensor I has a higher ME coefficient than sensor III which is related to its lower resonance frequency, resulting in a higher amplitude and thus higher ME coefficient under the same excitation magnetic field. In comparison to similar ME sensors from Marauska *et al* [11, 13] and Yarar *et al* [27], higher quality factors are achieved for all sensors. This fact can be explained mainly by the following two reasons. The sensors are vacuum encapsulated and the vacuum environment significantly reduces the air damping and thus enhances the quality factor [13, 14]. Secondly, a poly-Si substrate is integrated to the ME sensors, reducing the oscillation losses in resonance due to the ideal elastic properties of this material and a high Q is thus obtained. Other design related loss mechanisms such as anchor losses are crucial for an in-depth comparison of the different sensor types, but are outside the scope of this work.

The voltage noise density E of the investigated sensors is measured and shown in figure 7. The noise of the audio

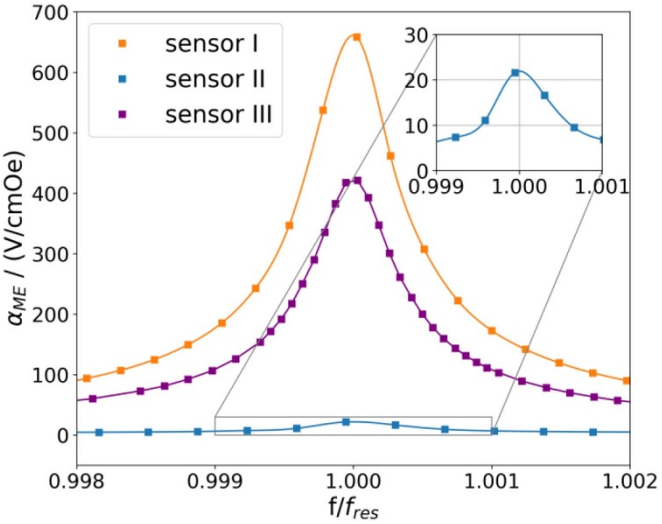

Figure 6. ME coefficient α_{ME} at the mechanical resonance (1st bending mode). Sensor I has a ME coefficient of 661 V cmOe^{-1} at 8200 Hz with a Q of 1800. Sensor II has a ME coefficient of 22 V cmOe^{-1} at 11 195 Hz with a Q of 1600. Sensor III has a ME coefficient of 424 V cmOe^{-1} at 13 043 Hz with a Q of 1900.

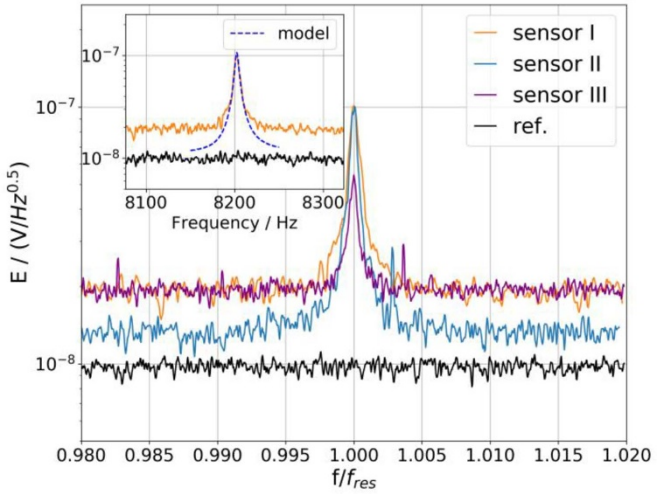

Figure 7. Voltage noise density spectra of sensor I, II and III were recorded at optimal magnetic bias field $|\mu H_{bias}| = 0.8$ mT, 0.5 mT and 0.9 mT, respectively. The noise of the audio interface is recorded as a reference. The noise density at resonance is determined as 101 nV/Hz$^{0.5}$ for sensor I, 100 nV/Hz$^{0.5}$ for sensor II and 54 nV/Hz$^{0.5}$ for sensor III. A comparison of measured and calculated noises [28] of sensor I is shown in the inset plot.

interface is measured as a reference which is sufficiently lower than the measured noise of the devices and thus can be neglected. At resonance, voltage noise densities of 101 nV/Hz$^{0.5}$, 100 nV/Hz$^{0.5}$ and 54 nV/Hz$^{0.5}$ have been measured for sensor I, II and III, respectively. The measurements show a distinct increase in noise at resonance for all three sensors, in agreement to thermal mechanical noise which is the dominant noise source for a cantilever sensor operated in its first bending mode [28].

Based on the electrical noise equivalent circuit of the ME sensor discussed by Durdaut *et al* in [28], a value of the

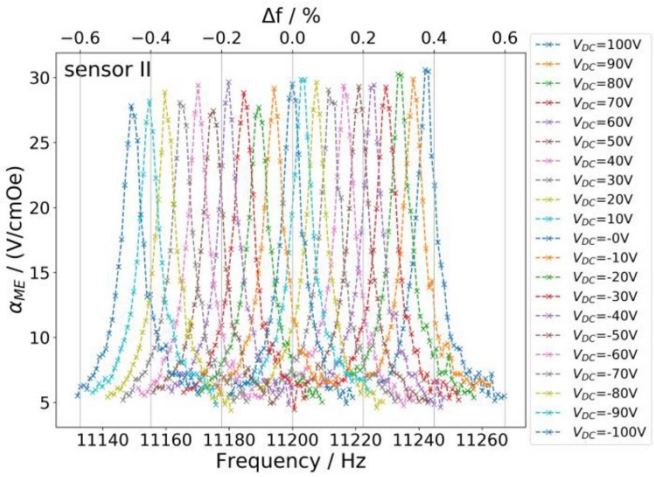

Figure 8. Measured ME coefficient α_{ME} of sensor II versus frequency for different applied DC voltages. The tuning of the resonance frequency of sensor II is about 0.41% per 100 V.

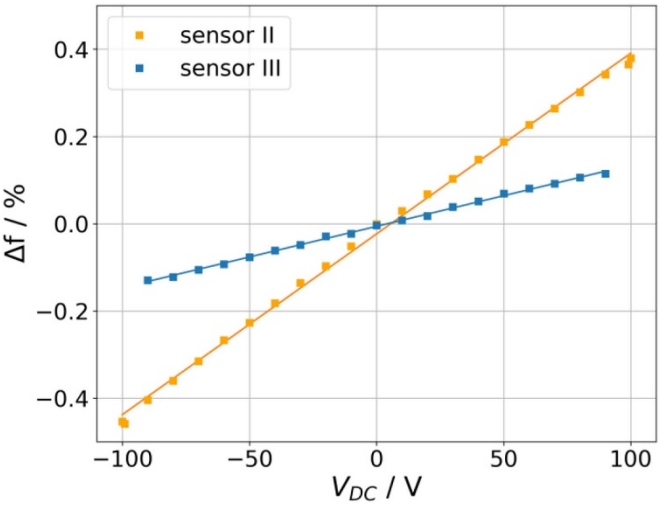

Figure 9. Change in resonance frequency of sensor II and III as a function of the applied tuning voltage. The frequency shift coefficients of 0.41% per 100 V and 0.14% per 100 V for sensor II and III are given by the different slopes.

intrinsic sensor noise can be derived. The calculated values of $E^{model}(f_{res})$ are in good agreement with measurements (figure 7 inset) not only for the single cantilever structure (sensor I, $E^{model}(f_{res}) = 105$ nV/Hz$^{0.5}$) but also for the more complex structures (sensor II and III, $E^{model}(f_{res}) = 96$ nV/Hz$^{0.5}$ and 40 nV/Hz$^{0.5}$, respectively).

From the values of the voltage noise density $E(f_{res})$ and ME voltage coefficient $\alpha_{ME}(f_{res})$, the limit of detection (LOD) can then be derived [9]:

$$LOD\,(f_{res}) = \frac{E\,(f_{res})}{t_{piezo} \cdot \alpha_{ME}\,(f_{res})} \tag{2}$$

Therefore, the LOD for sensor I is 153 pT/Hz$^{0.5}$, 4.6 nT/Hz$^{0.5}$ for sensor II and 128 pT/Hz$^{0.5}$ for sensor III. As all three sensors have been fabricated from the same wafer, t_{piezo} is the same for all sensors so that the relative changes in

Table 1. Measurement results of the investigated ME sensors. The parameters are resonance frequency, ME voltage coefficient $\alpha_{ME}(f_{res})$, voltage noise density $E(f_{res})$, quality factor Q, LOD and the frequency shift. All three sensors are characterized at an excitation field of 1 μT.

Sensor	$\lvert\mu H_{bias}\rvert$ (mT)	f_{res} (Hz)	$\alpha_{ME}(f_{res})$ (V cmOe^{-1})	$E(f_{res})$ (nV/Hz$^{0.5}$)	Q	LOD(f_{res}) (pT/Hz$^{0.5}$)	Δf (%/(100 V))	Δf (Hz/V)
I	0.8	8200	661	101	1800	153	–	-
II	0.5	11 195	22	100	1600	4563	0.41	0.5
III	0.9	13 043	424	54	1900	128	0.14	0.2

LOD are given by the ratio of the noise to ME coefficient only. High α_{ME}, lowest noise and in total best LOD are measured for sensor III. Although sensor I has the highest ME coefficient, the increase in noise yields a reduced LOD. The worst LOD is found for sensor II as expected.

To study the frequency tuning behaviour, an additional DC voltage is symmetrically applied (same voltage to both outer cantilevers) to the piezoelectric actuators of the tunable sensors II and III. All other measurement parameters are kept the same.

The ME coefficient of sensor II response to the applied voltage in resonance is plotted in figure 8. The resonance frequency of sensor II can be tuned as expected when a DC voltage is applied. With an increasing DC voltage from −100 V to 100 V (the bottom electrode is defined as ground), the resonance frequency of sensor II increases from 11 149 Hz to 11 243 Hz. The same qualitative tuning behavior is found for sensor III. The resonance frequency shift of sensor II and III with the applied tuning voltage is shown in figure 9. It reveals that both sensors show a linear tuning of the resonance frequency in the investigated voltage range. Sensor II has a frequency shift coefficient of 0.41% per 100 V which is about three times larger than the sensor III with a frequency shift of 0.14% per 100 V. Since sensor III has a clamped-free structure, the pre-stress on the structure generated by the applied voltage is partially released through displacement. Therefore, in comparison to sensor III, sensor II has a higher stress concentration on its double side clamped structure, resulting in a larger frequency shift. In particular, both sensors exhibit a highly reversible and hysteresis-free frequency tuning behavior, which is due to the linearity of the piezoelectric material AlN.

The measurement results of sensor I (reference sensor), II and III are summerized in table 1. It can be seen that sensor III has the best LOD which is by a factor of 36 lower compared to sensor II. Although sensor I has the highest ME coefficient of 661 V cmOe^{-1}, the LOD of sensor III is as good as the standard ME sensor. The frequency shift coefficients of 0.5 Hz V^{-1} and of 0.2 Hz V^{-1} are measured for sensor II and III respectively. However, the difference of the frequency shift coefficient between sensor II and III is not too large. As a result, sensor III with frequency tuning property shows an excellent performance comparable to the standard cantilever ME sensor.

To study the dependency of tuning on LOD and linearity of sensor III at resonance, the output voltage is measured as a function of external magnetic field for different tuning voltages (figure 10). Although the sensitivity (the slope of the linear regime) and the minimum detectable magnetic field vary slighly for different applied voltages (a LOD variation

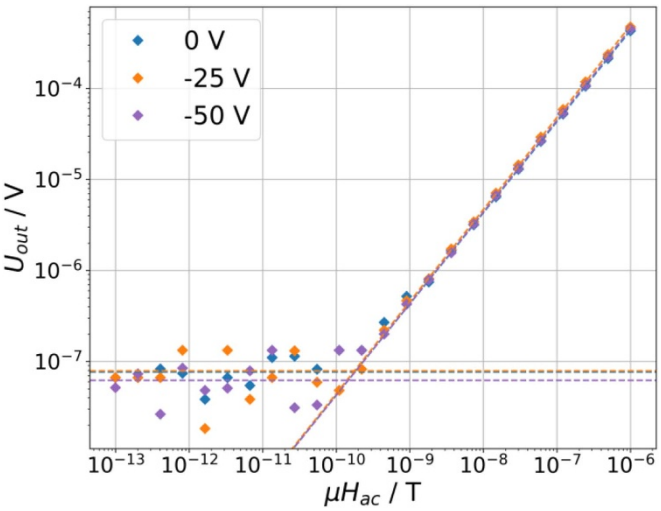

Figure 10. ME voltage of sensor III in dependence of external magnetic field μH_{ac} for different tuning voltages. The intersection of the linear response and the noise level indicates the minimum detectable magnetic field (LOD).

of ±32 pT/Hz$^{0.5}$ and a variation of sensitivity of ±43 V T^{-1} compared to the results without tuning), the linear response is highly preserved.

In comparison to the tunable ME sensors from Röbisch *et al* [21] and Wang *et al* [23], the presented sensor III has several distinct advantages in spite of a slightly higher limit of detection and a smaller frequency tuning. Based on its linear frequency tuning effect, the applied voltage, which can tune the resonance of the sensor to match the targeted frequency of the proposed applications, can be easily estimated. Due to its small size it can be easily assembled in flexible sensor arrays adaptable to different diagnostic requirements enabling better localization. In addition, it is suitable for mass production using MEMS technology.

5. Conclusion

In this study, we presented two vacuum encapsulated MEMS ME sensors with highly reversible quasi-linear frequency tuning effect. The presented frequency tuning method via integrated piezoelectric actuators can be easily controlled and is highly reproducible. Sensor II has a high frequency tuning coefficient of about 0.5 Hz V^{-1} with a LOD of 4.6 nT/Hz$^{0.5}$ while sensor III has a LOD of 128 pT/Hz$^{0.5}$ with a frequency tuning coefficient of about 0.2 Hz V^{-1}. In addition, the performance of sensor III for magnetic field sensing is not significantly affected by introducing piezoelectric tuning, which

enables ME sensors for measuring very weak magnetic fields with a precise control of the filter frequency (resonance). In summary, the combination of excellent performance for magnetic field detection and frequency tuning in a ME sensor was demonstrated which is highly beneficial for the development of vector field sensors and sensor arrays.

Acknowledgments

This work was funded by the German Science Foundation (DFG) through the Collaborative Research Centre CRC 1261 'Magnetoelectric Sensors: From Composite Materials to Biomagnetic Diagnostics'. The authors thank Lars Blohm for building up the measurement setup and Isa Pieper for supporting measurements. The authors thank Phillip Durdaut for helpful discussions about the noise model calculation.

ORCID iD

Jingxiang Su https://orcid.org/0000-0002-2994-2021

References

[1] Reermann J, Durdaut P, Salzer S, Demming T, Piorra A, Quandt E, Frey N, Höft M and Schmidt G 2018 Evaluation of magnetoelectric sensor systems for cardiological applications *Measurement* **116** 230–8
[2] Li M, Matyushov A, Dong C, Chen H, Lin H, Nan T, Qian Y, Rinaldi M, Lin Y and Sun N 2017 Ultra-sensitive NEMS magnetoelectric sensor for pico-Tesla DC magnetic field detection *Appl. Phys. Lett.* **110** 143510
[3] Zhai J, Xing Z, Dong S, Li J and Viehland D 2006 Detection of pico-Tesla magnetic fields using magneto-electric sensors at room temperature *Appl. Phys. Lett.* **88** 062510
[4] Friedrich R *et al* 2019 Magnetic particle mapping using magnetoelectric sensors as an imaging modality *Sci. Rep.* **9** 2086
[5] Nan T *et al* 2017 Acoustically actuated ultra-compact NEMS magnetoelectric antennas *Nat. Commun.* **8** 296
[6] Tavarozzi I, Comani S, Del Gratte C, Romani G L, Di Luzio S, Brisinda D, Gallina S, Zimarino M, Fenici R and De Caterina R 2002 Magnetocardiography: current status and perspectives. Part I: physical principles and instrumentation *Ital Heart J.* **3** 75–85
[7] Boto E *et al* 2018 Moving magnetoencephalography towards real-world applications with a wearable system *Nature* **555** 657–61
[8] Baillet S, Mosher J C and Leahy R M 2001 Electromagnetic brain mapping *IEEE Signal Process. Mag.* **18** 14–30
[9] Jahns R, Knöchel R, Greve H, Woltermann E, Lage E and Quandt E 2011 Magnetoelectric sensors for biomagnetic measurements *Proc. IEEE Int. Workshop Med. Meas. Appl. (MeMeA)* 107–10
[10] Srinivasan G 2010 Magnetoelectric composites *Annu. Rev. Mater. Res.* **40** 153–78
[11] Marauska S, Jahns R, Greve H, Quandt E, Knöchel R and Wagner B 2012 MEMS magnetic field sensor based on magnetoelectric composites *J. Micromech. Microeng.* **22** 065024
[12] Marauska S, Claus M, Lisec T and Wagner B 2013 Low temperature transient liquid phase bonding of Au/Sn and Cu/Sn electroplated material systems for MEMS wafer-level packaging *Microsyst. Technol.* **19** 1119–30
[13] Marauska S, Jahns R, Kirchhof C, Claus M, Quandt E, Knöchel R and Wagner B 2013 Highly sensitive wafer-level packaged MEMS magnetic field sensor based on magnetoelectric composites *Sensors Actuators* A **189** 321–7
[14] Kirchhof C, Krantz M, Teliban I, Jahns R, Marauska S, Wagner B, Knöchel R, Gerken M and Meyners D 2013 Giant magnetoelectric effect in vacuum *Appl. Phys. Lett.* **102** 232905
[15] Greve H, Woltermann E, Quenzer H J, Wagner B and Quandt E 2010 Giant magnetoelectric coefficients in $(Fe_{90}Co_{10})_{78}Si_{12}B_{10}$-AlN thin film composites *Appl. Phys. Lett.* **96** 182501
[16] Jahns R, Greve H, Woltermann E, Quandt E and Knöchel R 2012 Sensitivity enhancement of magnetoelectric sensors through frequency-conversion *Sensor Actuators* A **183** 16–21
[17] Salzer S, Höft M, Knöchel R, Hayes P, Yarar E, Piorra A and Quandt E 2015 Comparison of frequency conversion techniques for magnetoelectric sensor *Procedia Eng.* **120** 940–3
[18] Hayes P *et al* 2016 Electrically modulated magnetoelectric sensors *Appl. Phys. Lett.* **108** 182902
[19] Oswal A *et al* 2016 Analysis of simultaneous MEG and intracranial LFP recordings during deep brain stimulation: a protocol and experimental validation *J. Neurosci. Methods* **261** 29–46
[20] Salzer S, Jahns R, Piorra A, Teliban I, Reermann J, Höft M, Quandt E and Knöchel R 2016 Tuning fork for noise suppression in magnetoelectric sensors *Sensors Actuators* A **237** 91–95
[21] Röbisch V, Piorra A, Lima de Miranda R, Quandt E and Meyners D 2018 Frequency-tunable nickel-titanium substrates for magnetoelectric sensors *AIP Adv.* **8** 125320
[22] Petrie J R, Fine J, Mandal S, Sreenivasulu G, Srinivasan G and Edelstein A S 2011 Enhanced sensitivity of magnetoelectric sensors by tuning the resonant frequency *Appl. Phys. Lett.* **99** 043404
[23] Wang X, Zhao J, Xu B, Di W, Lu L, Hu F, Luo H and Gu H 2019 Theoretical model and experiments of resonance frequency shift by LC tuning in magnetoelectric sensor *Phys. Status Solidi* A **216** 1800966
[24] Su J, Niekiel F, Fichtner S, Kirchhof C, Meyners D, Quandt E, Wagner B and Lofink F 2019 Piezoelectric MEMS sensors for the detection of weak magnetic signals with adjustable resonance *MikroSystemTechnik Congress* pp 72–75
[25] Hrkac V, Lage E, Köppel G, Strobel J, McCord J, Quandt E, Meyners D and Kienle L 2014 Amorphous FeCoSiB for exchange bias coupled and decoupled magnetoelectric multilayer systems: real-structure and magnetic properties *J. Appl. Phys.* **116** 134302
[26] Durdaut P, Penner V, Kirchhof C, Quandt E, Knöchel R and Höft M 2017 Noise of a JFET charge amplifier for piezoelectric sensors *IEEE Sens. J.* **17** 7364–71
[27] Yarar E, Salzer S, Hrkac V, Piorra A, Höft M, Knöchel R, Kienle L and Quandt E 2016 Inverse bilayer magnetoelectric thin film sensor *Appl. Phys. Lett.* **109** 022901
[28] Durdaut P *et al* 2017 Thermal-mechanical noise in resonant thin-film magnetoelectric sensors *IEEE Sens. J.* **17** 2338–48